Hindawi
Geofluids
Volume 2022, Article ID 1452916, 14 pages
https://doi.org/10.1155/2022/1452916

Research Article

Experimental Study on the Triaxial Compression Properties of Coarse-Grained Filling Soil under Drying–Wetting Cycles

Shuyi Li,[1] **Zhilei He**,[2] **Peng Zhu**,[1] **Longxi Mei**,[1] **Shaojun Zeng**,[1] **and Siwei Wang**[2]

[1]*Huadong Engineering Corporation Limited, Hangzhou 310000, China*
[2]*North China University of Water Resources and Electric Power, Zhengzhou 450045, China*

Correspondence should be addressed to Shuyi Li; li_sy@hdec.com and Siwei Wang; wsw@ncwu.edu.cn

Received 7 July 2022; Revised 16 October 2022; Accepted 26 October 2022; Published 14 November 2022

Academic Editor: Quanle Zou

To explore the mechanical properties of coarse-grained filling soil in the hydrofluctuation belt of the Baihetan reservoir, a fast drying–wetting cycle method for large-scale triaxial tests was developed and a series of large-scale triaxial compression tests of coarse-grained soil were conducted under drying–wetting cycles. The results show that the drying–wetting cycles and the confining pressure are both important factors affecting the mechanical properties of coarse-grained soil. The influences of the first and second cycles on the deviatoric stress–strain curve of the coarse-grained soil are the greatest, while the influences of the third to seventh cycles tend to be stable. The peak strain is not affected by the drying–wetting cycles but only increases with increasing confining pressure. The axial strain and volumetric strain at the volume expansion point decrease with increasing number of drying–wetting cycles but increase with increasing confining pressure. The secant modulus of the peak point decreases with increasing number of drying–wetting cycles, and the initial tangent modulus decreases slightly. The influence of the drying–wetting cycles on the cohesion of the coarse-grained soil is greater than that on the internal friction angle. The typical "bulging" phenomenon occurred after the specimens were destroyed. A damage constitutive equation was developed by introducing a damage variable into the hyperbolic model to reflect the influence of the number of drying–wetting cycles. The model parameters were obtained and the proposed model was verified by fitting the experimental results.

1. Introduction

The Baihetan hydropower station is the largest hydropower station under construction in the world. The dam site is located on the Jinsha River between the Sichuan and Yunnan provinces, approximately 41 km from Qiaojia County in Yunnan Province. The normal storage water level is 825 m, the dead water level is 765 m, and the backwater length of the main stream is approximately 182 km. A large number of villages and farmland were submerged following the storage of water in the dam. To relieve the shortage of land in the reservoir area, a large number of filling areas were built along the river. The filling areas are formed from compacted coarse-grained soil filling material. Because of the short filling time, the internal structure of the filling material is not completely stable and further settlement will occur under the action of gravity. In addition, the water level fluctuates periodically between the flood limit water level and the normal water level every year to generate electricity. The height of the hydrofluctuation belt is up to 60 m. The filling material in the hydrofluctuation belt will therefore experience drying–wetting cycles for a long time. The structural evolution process of the filling material will inevitably change and have an important impact on the deformation and stability of the filling area. Therefore, it is important to study the mechanical properties of the filling material in the water-level-fluctuation zone.

The drying–wetting cycle process reflects the cyclic water loss and water-saturation process of the soil. Many studies [1–8] have been conducted on indoor drying–wetting cycle tests and simulation methods. However, there is no one uniform test method at present as a result of the many types of rock and soil, their various properties, and the difficulties associated with drying–wetting treatments, as well as other reasons.

In general, small samples of fine-grained soil can be used to simulate the drying–wetting cycle process according to the moisture content index. For example, samples with a high moisture content after being saturated are regarded as being in the "wet" state and samples with low moisture content after drying naturally for a period of time are regarded as being in the "dry" state. To truly simulate the dry and wet states of an engineering site and to speed up the process of air-drying samples, the current commonly-used test method is to place the soil in a wet state via natural soaking and in a dry state via drying in a temperature and humidity controlled box. The temperature and humidity are set to the actual temperature and humidity conditions at the engineering site [9–12].

However, this test method is not suitable for large-scale samples of coarse-grained soil. Large samples are usually heavy and difficult to move. Furthermore, large samples cannot be dried in temperature and humidity controlled boxes. As a result of the strong permeability of coarse-grained soil, a common drying–wetting cycle test method for coarse-grained soil is realized via natural soaking and natural air drying. According to ASTM D599, a drying–wetting cycle for soil–cement includes 2 days of soaking and 2 days of drying. However, some scholars regard 1 day of soaking and 1 day of drying as a single drying–wetting cycle [13, 14]. In this method, the filling material in the filling area is granular and the sample is assembled directly in a rubber film. Because the rubber film is closed, natural air drying can only be accomplished in the upper and lower regions of the sample. It is difficult to lose water in the middle of the sample; consequently, the drying effect is poor in this region. Therefore, it is necessary to develop a fast drying–wetting cycle test method for large-scale triaxial compression tests of filling materials.

Over the past few decades, the effects of drying–wetting cycles on various soils have been investigated; investigated soils include cement-improved argillite-slate coarse-grained soil [13], basalt fiber-reinforced loess [15], expansive soil [16, 17], silty clay [18], and red sandstone [19, 20]. In general, it has been found that drying–wetting cycles cause the soil structure to become damaged, weakening the physical and mechanical properties of the soil. With increasing number of drying–wetting cycles, the strength decreases successively, obviously in the first four cycles and gradually after the fifth cycle. The effect of the drying–wetting cycles on the cohesion is obviously greater than that on the internal friction angle. Because a coarse-grained soil filling material is not consolidated, the degradation of its mechanical properties is highly significant and complex in a drying–wetting cycle. By far, the research has not been seen in the domestic reports. Therefore, it is necessary to research the mechanical properties of coarse-grained soil filling materials under drying–wetting cycles.

This paper investigates the influence of drying–wetting cycles on the filling materials in the Beimen filling engineering site of the Baihetan reservoir area. The basic physical properties of the filling material are analyzed, and a type of coarse-grained soil indoor large-scale triaxial test drying–wetting cycle test method is proposed. The deformation behavior and shear strength are obtained from a series of large-scale triaxial compression tests. It is important to establish a damage constitutive model based on the number of drying–wetting cycles and to analyze the deformation and stability of the filling materials in the water-level-fluctuation zone of the reservoir area.

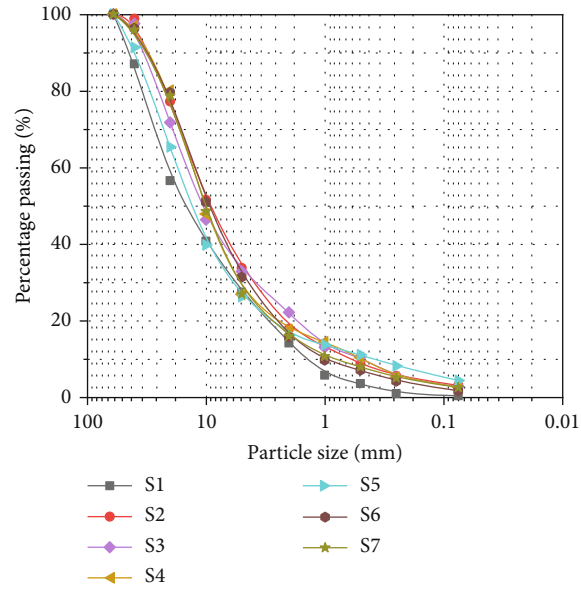

Figure 1: Grain size distribution curve of the coarse-grained filling soil.

Figure 2: Triaxial testing system (SZLB-4).

2. Basic Characteristics of the Filling Materials in Qiaojia County

The filling material in the Beimen filling area is primarily sourced from the water military river quarry in Qiaojia County in the Baihetan reservoir area, which primarily consists of gravel, breccia, and silty clay. In the indoor large-scale conventional triaxial test, the effect of the sample size is considered and particles with sizes greater than 60 mm are eliminated. The grain distribution curve is shown in Figure 1. The corresponding uniformity coefficient and the curvature coefficient are 21–55 and 1.28–3.56, respectively, and the filling materials are categorized as well-graded coarse-grained soil.

(a) First saturation (b) Subsequent saturation (c) Complete saturation

Figure 3: Sample saturation.

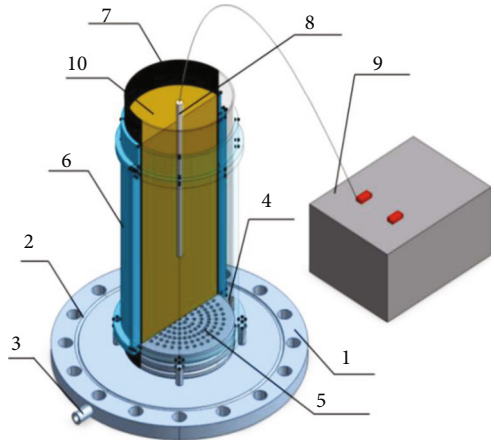

1 Base
2 Rubber waterstop
3 Drainage holes
4 Water injection hole
5 Triaxial pressure cell
6 Open-ended sample kit
7 A rubber film
8 A built-in heating rod
9 A temperature-control system
10 Soil sample

Figure 4: Heating device for the samples.

3. Test Program Design

3.1. Test Equipment. The large-scale triaxial tests of the coarse-grained soil under drying–wetting cycles were conducted using an SZLB-4 stress-type triaxial testing machine to enable a confining pressure and an axial load; these were controlled via the real-time servo of the test system, as shown in Figure 2.

3.2. Test Procedure and Design. Large-scale triaxial consolidated drained (CD) test method was adopted in the triaxial test process of coarse-grained soil under drying and wetting cycles in the paper. Compared with the conventional triaxial test, the most significant difference is that soil samples have to be treated by the –t cycle, test procedure were as follows.

3.2.1. Sample Preparation. Diameter and height of the specimens is $\Phi 300\,\text{mm} \times 600\,\text{mm}$. The samples were prepared via compaction in 10 cm layers, with the density controlled at $2.3\,\text{g/cm}^3$. According to the volume of the forming cylinder, the coarse-grained soil materials were weighed and placed into the forming cylinder covered with a rubber film. A hammer was used for the compaction. After compaction to the control target height, the surface unevenness was resolved using a scraper. The second to sixth layers were then tamped via the same method.

(a) Layout of the heating rod and the temperature-control probe (b) Drying effect after heating

Figure 5: Sample drying.

Table 1: Triaxial test scheme of the coarse-grained soil under drying–wetting cycles. *N* denotes the natural state, *S* denotes the saturation state, and DW2 – 7 denote the second to seventh drying–wetting cycles.

No.	Confining pressure (kPa)			
	100	200	300	400
1	*N*	*N*	*N*	*N*
2	*S*	*S*	*S*	*S*
3	DW2	DW2	DW2	DW2
4	DW3	DW3	DW3	DW3
5	DW4	DW4	DW4	DW4
6	DW5	DW5	DW5	DW5
7	DW6	DW6	DW6	DW6
8	DW7	DW7	DW7	DW7

(a) Bulging deformation (b) Large broken particles

Figure 6: Failure behavior.

3.2.2. Sample Saturation. The samples were saturated via water injection. The samples were connected to tap water via a water injection hole in the chassis of the triaxial pressure cell. The speed of water injection was controlled to expel as much of the gas in the triaxial cell as possible. To fully saturate the soil, the water surface needs to exceed the upper surface of the soil sample by 10 cm in the first saturation, as shown in Figure 3(a). The water surface then needs to exceed the soil sample by 5 cm in the subsequent saturation, as shown in Figure 3(b). The first saturation time was greater than 3 h, and the subsequent saturation time was greater than 2 h. After saturation was complete, there was still a small amount of water stored on the surface of the sample. Once the target saturation

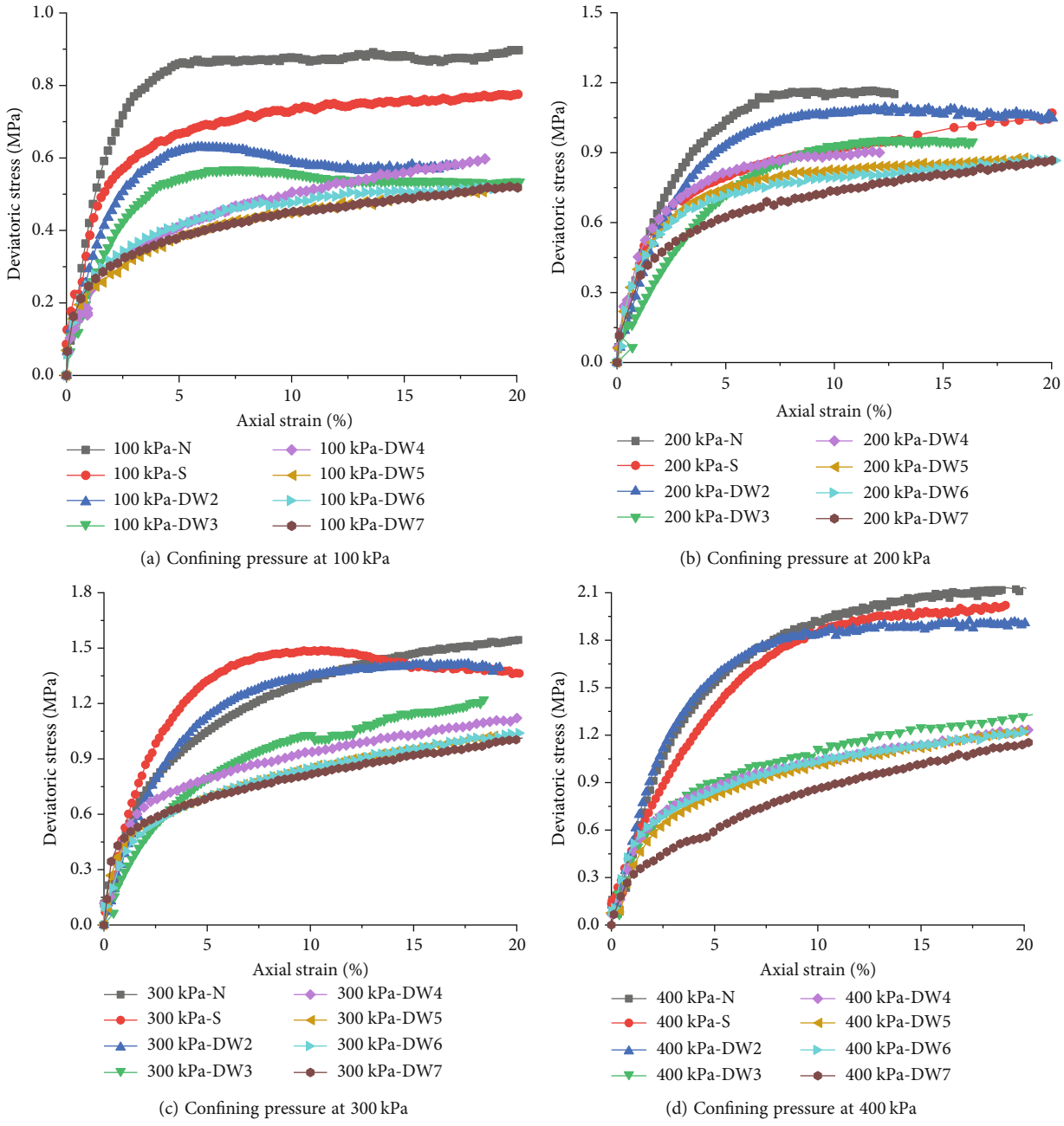

(a) Confining pressure at 100 kPa

(b) Confining pressure at 200 kPa

(c) Confining pressure at 300 kPa

(d) Confining pressure at 400 kPa

Figure 7: Stress–strain curves under drying–wetting cycles for various confining pressures.

time was reached, the upper and lower drainage holes were opened; a saturated sample is shown in Figure 3(c).

3.2.3. Sample Drying. The sample drying procedure was different from that of ordinary small samples. Because of the large size and weight of the samples, it was impossible to directly place the samples into a drying oven. Drying the sample using conventional natural drying would take a long time. Following conventional natural drying, the sample was still very wet after 21 days and the water-loss effect of the sample was not obvious. The sample could be dried by adding an external electromagnetic heating ring outside the triaxial cell. In such a configuration, the temperature of the heating ring can reach 300°C. However, because the soil samples have poor thermal conductivity, it is difficult to transfer heat energy from the triaxial cell or from the outside of the sample to the interior of the sample. After heating for 24 h, the amount of water loss was small and the drying effect was poor. Accordingly, a new drying method for large-scale triaxial tests of coarse-grained soil is proposed in this paper. The heating device is shown in Figure 4. To improve the drying effect, the soil sample is heated using a built-in heating rod. The length of the heating rod was 65 cm and its diameter was 1 cm. An electric pick was used to make holes in the central area of the sample, and then a heating rod with a temperature-control system was inserted to dry the sample. The temperature-control probe was inserted into the soil approximately 12 cm from the heating rod. To prevent the soil around the heating rod from being overheated, the temperature

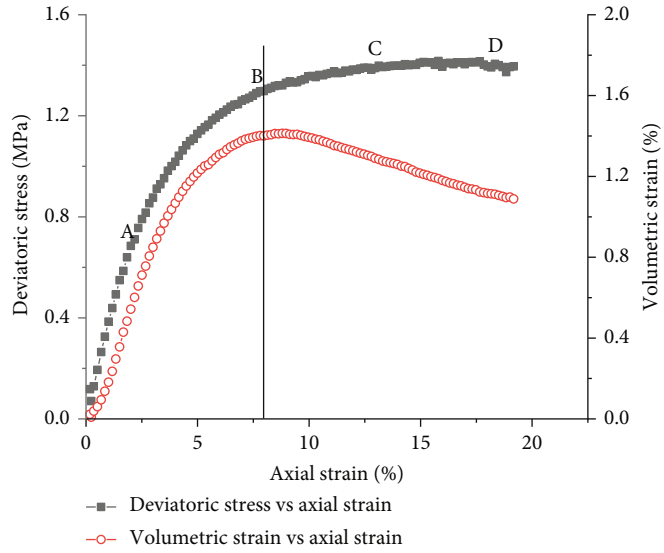

Figure 8: Typical deviatoric stress–strain and volumetric strain–strain curves.

Table 2: Initial tangent modulus and peak point secant modulus.

Sample	Initial tangent modulus (MPa) Confining pressure (MPa)				Peak point secant modulus (MPa) Confining pressure (MPa)			
	0.1	0.2	0.3	0.4	0.1	0.2	0.3	0.4
N	29	35	45	50	18	16	13	15
S	25	35	44	45	14	12	14	15
DW2	23	29	33	44	12	12	12	13
DW3	18	15	25	36	12	12	11	9
DW4	14	27	29	31	9	11	9	8
DW5	14	27	29	31	9	11	8	8
DW6	14	27	29	31	8	10	8	8
DW7	14	27	29	31	7	9	8	8

is controlled at 90°C. If the temperature near the probe exceeds this value, the heating rod automatically shuts down. When the temperature is lower than this value, the heating rod automatically turns on. Figure 5(a) shows the layout of the heating rod and the temperature-control probe, and Figure 5(b) shows the drying effect after heating.

3.2.4. Test Scheme Design. A total of 32 triaxial compression tests were performed under drying–wetting cycles; these tests were divided into 8 groups. The sample states were the natural state, the saturated state, and the second to seventh drying–wetting cycles. The natural and saturated tests can be regarded as the first drying–wetting cycle. The samples were assembled according to the natural water content. The sequence saturated, dried, and then saturated was regarded as a single drying–wetting cycle. The specific test scheme is shown in Table 1.

3.2.5. Confining Pressure Setting. The triaxial test confining pressure design is 100, 200, 300, and 400 kPa, and the loading rate is 50 N/s. The axial stress is applied according to the deformation control, and the loading rate is 1 mm/min. According to the suggestions of geotechnical related test regulations, standard for geotechnical testing method (GB/T 50123-2019), when there is a peak value, the test should be carried out to 3%-5% after the axial strain reaches the peak value. If there is no peak value, the axial strain reaches 15%-20%.

4. Test Results and Analysis

4.1. Failure Characteristics. The specimen displayed a typical bulging phenomenon following failure. In this phenomenon, the lateral expansion of the middle part of the sample is obvious and the lateral deformations of the top and bottom ends are small, as shown in Figure 6(a). Large broken particles can be observed after dissection, as shown in Figure 6(b).

4.2. Deformation Characteristics

4.2.1. Deformation Characteristics under Different Drying–Wetting Cycles

(1) Overall Distribution Characteristics of the Stress–Strain Curves. Under the same confining pressure, the deviatoric stress–strain curves of the coarse-grained soil under different drying–wetting cycles are shown in Figure 7. The test results

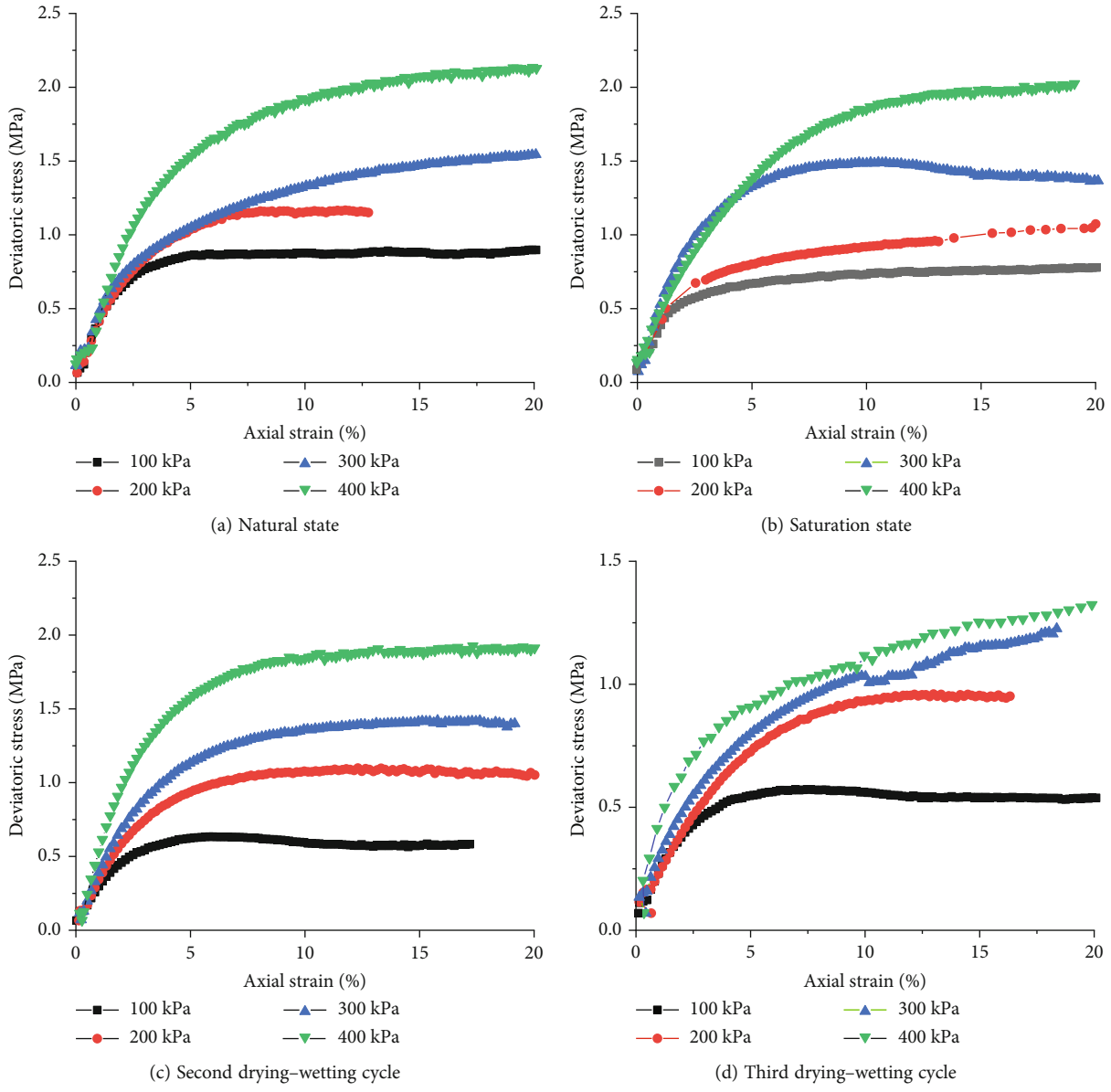

Figure 9: Continued.

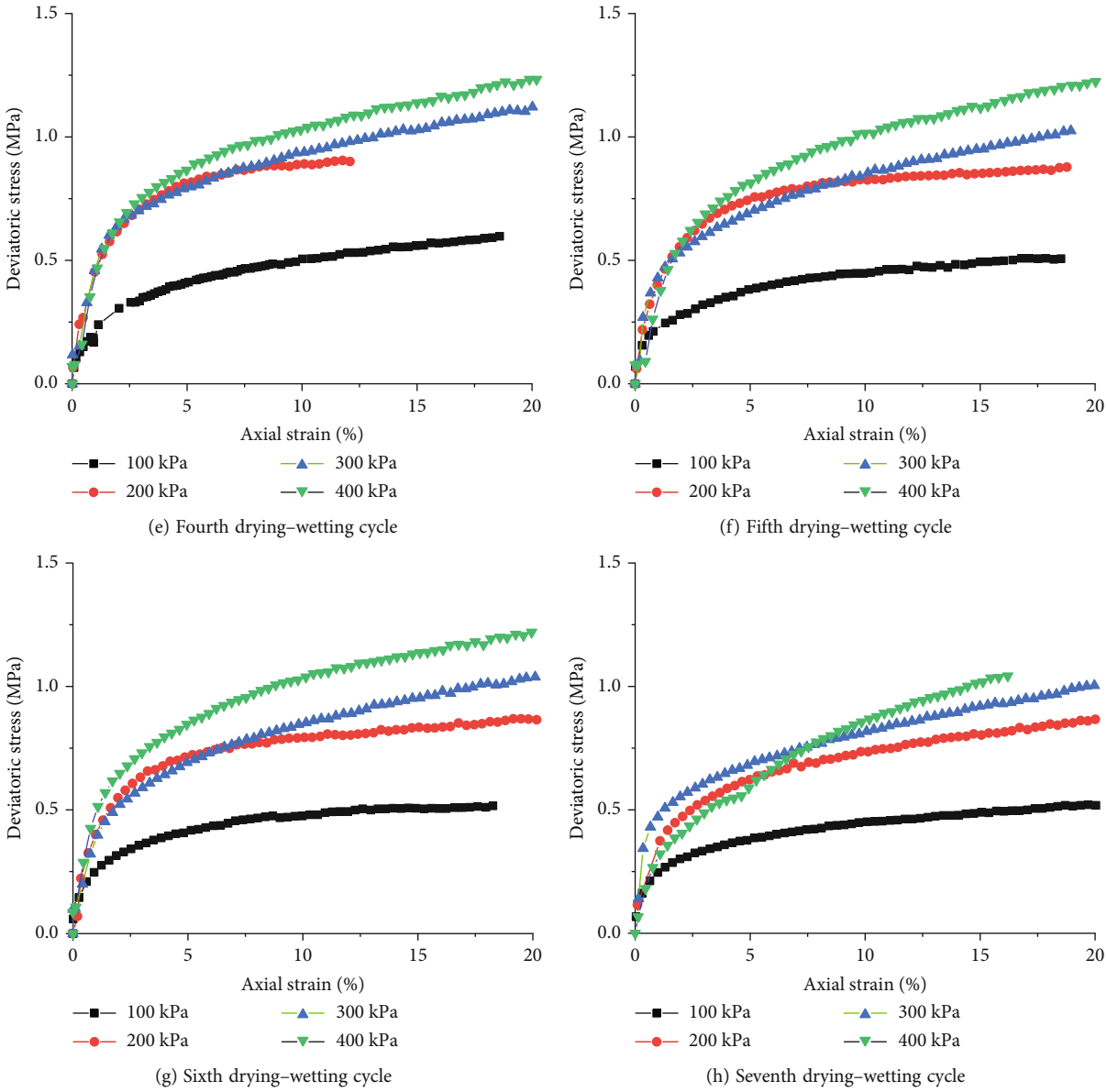

Figure 9: Stress–strain curves following different numbers of drying–wetting cycles.

indicate that the general characteristics of the deviatoric stress–strain curves of the coarse-grained soil are similar under the same confining pressure and different drying–wetting cycles. A typical deviatoric stress–strain curve of the coarse-grained soil under triaxial stress is primarily distributed in an approximately linear ascending segment (OA), a curved ascending segment (AC), and an approximately horizontal segment (CD), as shown in Figure 8. In the approximately linear ascending segment OA, the deviatoric stress increases approximately linearly with the axial strain and the sample volume is compressed, reflecting approximately elastic behavior. The ascending segment of the AC curve can be further divided into an AB segment and a BC segment. In the AB section, the deviatoric stress increases nonlinearly with increasing axial strain and the volume of the sample is compressed. Small cracks begin to appear in the sample but are rupture stable. At point B, the sample volume is compressed to its minimum and then the sample transitions from compression to expansion. Accordingly, point B is called the volume expansion point. After point B, the specimen transitions from stable fractures to unstable fractures. The stress of the specimen can still increase; however, it is close to the peak stress level. At this stage, the deformation increases sharply and the stress increases slowly. After reaching the peak point C, the strain continues to increase and the stress remains basically stable. The stress–strain curve becomes approximately level, reflecting an ideal plasticity state.

(2) Peak Strain. The peak strain of the deviatoric stress–strain curve of the coarse-grained soil is basically the same under the same confining pressure and different drying–wetting cycles. That is, it is not affected by the number of drying–wetting cycles experienced by the sample. Because the peak point of the deviatoric stress–strain curve is not obvious, we define the peak point as the point where the

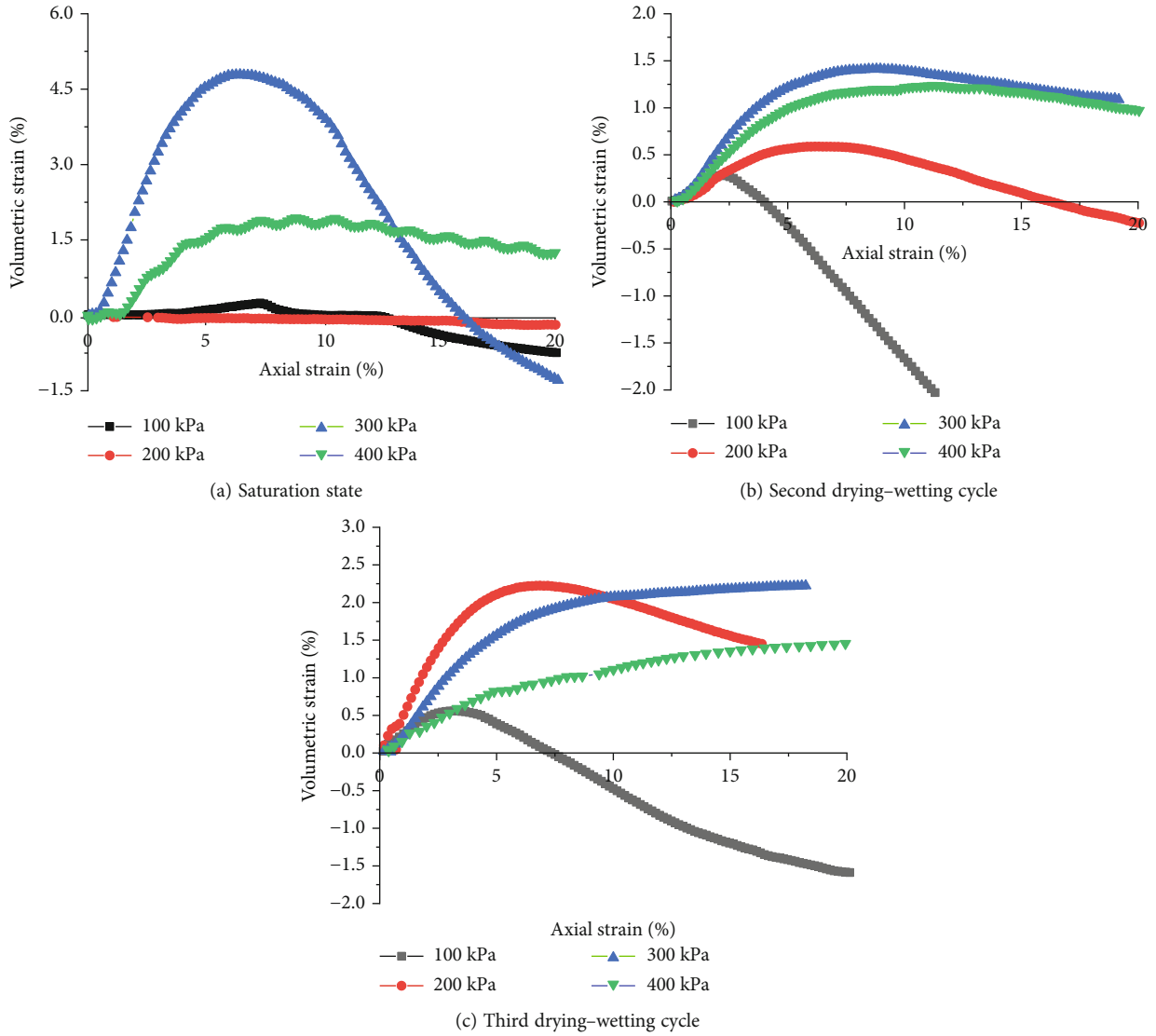

Figure 10: Volumetric strain–axial strain curves under different confining pressures and the same number of drying–wetting cycles.

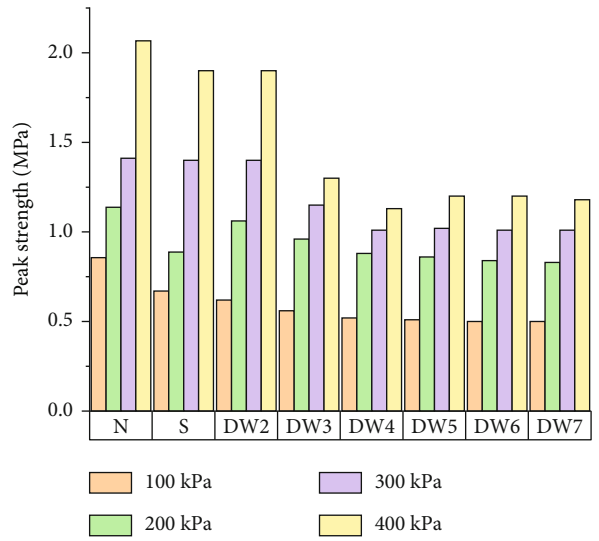

Figure 11: Strength under various drying–wetting cycle conditions.

Table 3: Strength and indexes under drying–wetting cycle.

Sample	Deviatoric stress (kPa)				Cohesion (kPa)	Frictional angle (°)
	100	200	300	400		
N	860	1140	1410	2070	79.2	43.4
S	670	890	1400	1900	36.2	42.6
DW2	620	1060	1360	1900	34.1	42.4
DW3	560	960	1150	1300	35.6	42.1
DW4	520	880	1010	1130	33.0	41.5
DW5	510	860	1020	1200	31.2	40.3
DW6	500	840	1010	1200	31.0	40.1
DW7	500	830	1010	1180	30.8	40.0

maximum stress first appears; the corresponding strain is then the peak strain. Under the four confining pressures of 100, 200, 300, and 400 kPa, the peak strain is basically the same after going through the natural and saturated states and the second to seventh drying–wetting cycles; the peak strain values are approximately 5%, 7%, 9%, and 11%, respectively.

(3) Initial Tangent Modulus and Peak Point Secant Modulus. According to the deviatoric stress–strain curves of the coarse-grained soil under the same confining pressure and different drying–wetting cycles, the initial section of the curve is an approximately straight upward section. The slope of this section can be used as the initial tangent modulus. The slope between the peak point and the origin can be used as the secant modulus of the peak point. The initial tangent modulus and the peak point secant modulus of the coarse-grained soil under different drying–wetting cycles under the same confining pressure are listed in Table 2. It can be seen that, as the number of drying–wetting cycles increases, the initial tangent modulus of the coarse-grained soil tends to decrease gradually under the same confining pressure; however, the degree of this decrease is small. For example, under a confining pressure of 100 kPa, with the change of the sample from natural to saturated and the second to seventh drying–wetting cycles, the initial tangent modulus decreases from 29 MPa to 25 MPa, 23 MPa, 18 MPa, and 14 MPa, respectively; however, each decrease is small with a range of 0–4 MPa. After the first drying–wetting cycle, the decrease is the most obvious, while later decreases are smaller. This indicates that, as the number of drying–wetting cycles increase, the slope decreases but the change is not obvious. When the confining pressure is 200 kPa, 300 kPa, or 400 kPa, the trend is the same as that at 100 kPa but with higher values.

4.2.2. Deformation Characteristics under Different Confining Pressures

(1) Overall Distribution Characteristics of the Stress–Strain Curves. Figure 9 shows the deviatoric stress–strain curves of the coarse-grained soil under different confining pressure conditions and the same drying–wetting cycle conditions. The test results show that, under the same drying–wetting cycle conditions, the overall characteristics of the deviatoric stress–strain curves of the coarse-grained soil remain the same with increasing confining pressure. The deviatoric stress–strain curves are primarily distributed in an approximately straight upward section, a curved upward section, and an approximately horizontal section. There are no obvious peak points or obvious downward sections, reflecting approximately ideal plasticity. The approximately straight upward section, peak stress, and peak strain of the deviatoric stress–strain curve of the coarse-grained soil increase when the confining pressure increases from 100 kPa to 200 kPa, 300 kPa, and 400 kPa. After reaching its peak, all the curves reflect approximately ideal plasticity.

(2) Volume Deformation Characteristics. Figure 10 shows the volumetric strain–axial strain curves of typical coarse-grained soils under different confining pressures and the same number of drying–wetting cycles.

The test results show that the overall distribution characteristics of the volumetric strain–axial strain curves of the specimens are similar, even under different confining pressures. In summary, the volumetric strain increases with increasing axial strain until the maximum value and then begins to rebound. That is, the initial state of the sample is compression with increasing axial compression. The sample begins to expand when the volume of the sample reaches its minimum value. The point of the minimum volume is called the volume expansion point, and the volume expansion point appears prior to the peak stress.

4.3. Strength Characteristics

4.3.1. Peak Strength. Figure 11 shows the triaxial compressive strength of the coarse-grained soil under different confining pressures and different drying–wetting cycle conditions. The drying–wetting cycle conditions and the confining pressure significantly affect the triaxial compression strength of the coarse-grained soil.

The test results indicate that the shear strength distribution characteristics of the coarse-grained soil are different under the same confining pressure and different drying–wetting cycle conditions. The influence of the drying–wetting cycles on the shear strength is divided into three stages. The first stage is

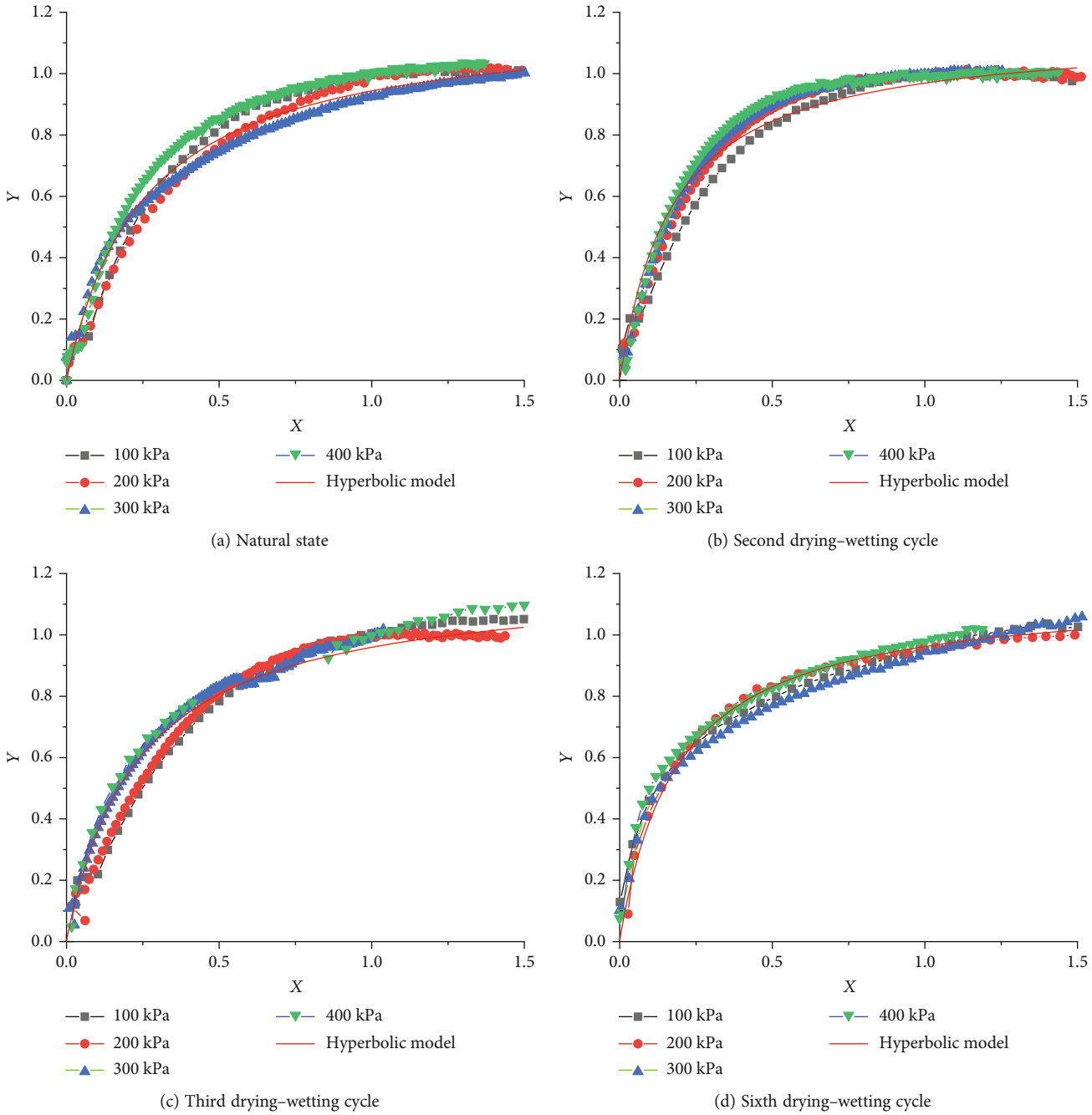

(a) Natural state

(b) Second drying–wetting cycle

(c) Third drying–wetting cycle

(d) Sixth drying–wetting cycle

Figure 12: Fitting results of the hyperbolic model.

the nature state. The second stage is the first and second drying–wetting cycles. The third stage is the three to seven drying–wetting cycles. The strength of the natural state is higher than that of the first and second drying–wetting cycles. After going through three to seven drying–wetting cycles, the strength tends to become stable.

4.3.2. Shear Strength Indexes. The first principal stress and the third principal stress of coarse-grained soil conform to Mohr-Coulomb failure criterion under the same drying–wetting cycle conditions. The shear strength and shear strength index of coarse-grained soil under different drying–wetting cycles are shown in Table 3. The results show that the shear strength of coarse-grained soil increases with the increasing confining pressure at the same number of drying–wetting cycles. The number of drying–wetting cycles had significant influence on the cohesion of shear strength index of coarse-grained soil. The natural and the first saturation states were the most affected. When the drying–wetting cycles were carried out to the second to seventh times, its influence was significantly reduced. The number of drying–wetting cycles has little effect on the internal friction angle of shear strength index of coarse-grained soil. The cohesion of coarse-grained soil in natural state is 79.2 kPa. After going through the first to fourth drying–wetting cycles, the

Table 4: Fitting values of the hyperbolic model.

	N	S	DW2	DW3	DW4	DW5	DW6	DW7
a	0.21	0.18	0.16	0.20	0.19	0.19	0.17	0.21
b	0.84	0.86	0.88	0.81	0.82	0.84	0.87	0.85
R^2	0.98	0.97	0.98	0.98	0.97	0.97	0.96	0.96

Table 5: Secant modulus and damage variable under a given number of drying–wetting cycles.

Sample	100 kPa		200 kPa		300 kPa		400 kPa	
	E (MPa)	D_N	E (MPa)	D_N	E (MPa)	D_N	E (MPa)	D_N
N	17.75	0	15.81	0	12.95	0	15.47	0
S	13.76	0.22	12.16	0.23	11.96	0.08	14.51	0.06
DW2	12.37	0.30	14.57	0.08	11.86	0.08	13.41	0.13
DW3	10.8	0.39	11.84	0.25	9.55	0.26	9.36	0.40
DW4	8.35	0.53	11.07	0.30	9.09	0.30	8.30	0.46
DW5	8.67	0.51	10.89	0.31	8.57	0.34	8.45	0.45
DW6	8.06	0.54	10.37	0.34	8.02	0.38	8.11	0.47
DW7	7.35	0.59	9.65	0.39	7.71	0.40	7.52	0.51

values are 36.2, 34.1, 35.6, and 33.0 kPa, which are 46%, 43%, 45%, and 42% of the natural state, respectively. The internal friction angle changed from 43.4° in natural state to 42.6°, 42.4°, 42.1°, and 41.5°, which were 98%, 98%, 97%, and 96% of those in the natural state, respectively.

5. Damage Constitutive Model of Coarse-Grained Soil under Drying–Wetting Cycles

5.1. Test Data Preprocessing. According to the results of the triaxial compression tests of the coarse-grained soil filling material, when the maximum stress value is reached on the axial deviatoric stress–strain curve for the first time, the maximum value, called the peak stress or peak strength, is denoted as σ_f and the strain corresponding to the peak stress, called the peak strain, is denoted as ε_f. The axial deviatoric stress is denoted as $\sigma_1 - \sigma_3$ and the axial strain is denoted as ε_1. Let $x = \varepsilon_1/\varepsilon_f$ and $y = (\sigma_1 - \sigma_3)/\sigma_f$. The axial deviational stress–strain curves of the coarse-grained soil under different drying–wetting cycles can then be transformed and plotted with respect to x and y; some representative results are shown in Figure 12.

According to Figure 12, the distribution characteristics of the normalized deviator stress–strain curves are very similar and the confining pressure has no notable influence on the deviator stress–strain curves. An analysis of the deformation law of the coarse-grained soil indicates that both the number of drying–wetting cycles and the confining pressure are the two main factors affecting the strength and deformation of the soil. Therefore, after data normalization, the deviatoric stress–strain curve is primarily affected by the number of drying–wetting cycles. According to the characteristics of the deviatoric stress–strain curve after preprocessing, it was found that the curve can be described by a hyperbolic model and that its equation can be expressed as

$$y = \frac{x}{a + \mathrm{bx}}, \tag{1}$$

where a and b are the model parameters.

The normalized deviatoric stress–strain curves were fitted using the hyperbolic model to obtain the a and b parameters. The results are shown in Table 4 and the fitted results are shown in Figure 12. The fitting effect is good and the fitted curve is basically consistent with the test curve.

Because $x = \varepsilon_1/\varepsilon_f$ and $y = (\sigma_1 - \sigma_3)/\sigma_f$, the hyperbolic model can be written as

$$\sigma_1 - \sigma_3 = \frac{\varepsilon\sigma_f}{a\varepsilon_f + b\varepsilon_1}. \tag{2}$$

5.2. Damage Constitutive Model. In the process of water absorption and water loss, the structure of the coarse-grained soil changes, resulting in damage and a decrease in the mechanical properties of the soil. According to Section 4.2, the secant modulus of the peak point is the slope between the peak point and the origin of the deviatoric stress–strain curve. The change in this value reflects the influence of the drying–wetting cycles and the damage degree of the internal structure. This value is not significantly affected by the confining pressure. Therefore, according to the test results, the change in the secant modulus can be used to represent the damage to soil subjected to drying–wetting cycles. If D_N represents the

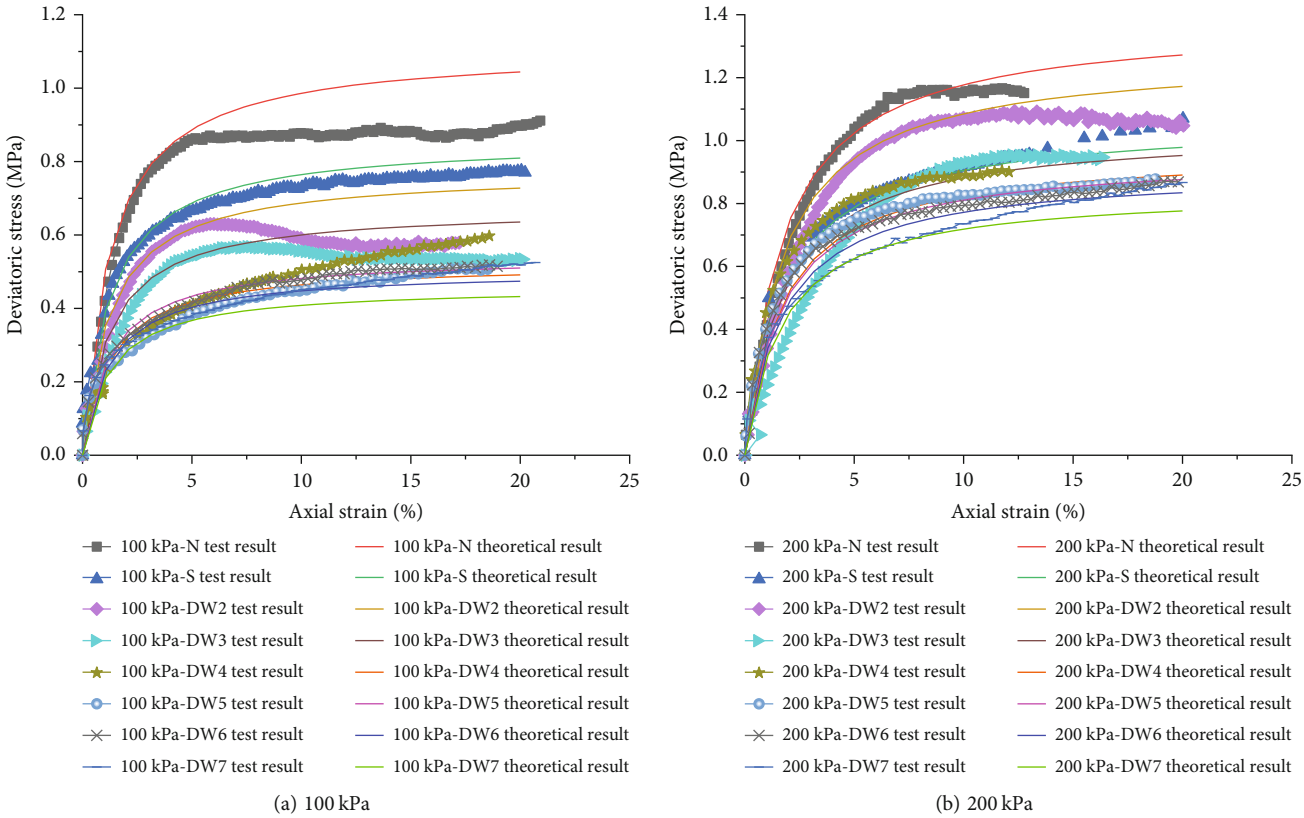

(a) 100 kPa (b) 200 kPa

Figure 13: Contrast between the test results and the theoretical results for two different confining pressures.

damage variable after N drying–wetting cycles, the damage can be expressed as

$$D_N = 1 - \frac{E_N}{E_0}, \tag{3}$$

where E_N is the peak point secant modulus after N drying–wetting cycles and E_0 is the peak point of the secant modulus in the natural state.

The peak stress after N drying–wetting cycles can be written as

$$\sigma_f = E_N \varepsilon_f = E_0(1 - D_N)\varepsilon_f, \tag{4}$$

where σ_f is the peak stress after N drying–wetting cycles and ε_f is the peak strain after N drying–wetting cycles.

Substituting Equations (3) and (4) into Equation (2), the damage constitutive model can be written as

$$\sigma_1 - \sigma_3 = \frac{\varepsilon_1 \sigma_f}{a\varepsilon_f + b\varepsilon_1} = \frac{\varepsilon_1 E_0(1 - D_N)\varepsilon_f}{a\varepsilon_f + b\varepsilon_1}.. \tag{5}$$

5.3. Model Parameters and Verification. With the increasing number of drying–wetting cycles, the secant modulus gradually decreases and the damage variable gradually increases. According to the test results, the change law of the secant modulus E and the damage variable D_N given the number of drying–wetting cycles is shown in Table 5.

According to the previous analysis of the deformation characteristics of the different drying–wetting cycles, the maximum strain is closely related to the confining pressure but not to the number of drying–wetting cycles. Therefore, to establish damage constitutive models of coarse-grained soil under different confining pressures and different drying–wetting cycles, it is necessary to establish the relationship between the confining pressure and the maximum strain. According to the test results of the coarse-grained soil under different confining pressures, the maximum strain can be assumed to be a constant value under the same confining pressure. The stress–strain relationship of the coarse-grained soil under different drying–wetting cycles can be obtained using Equation (5). Taking confining pressures of 100 kPa and 200 kPa as examples, the theoretical results can be compared with the test results, as shown in Figure 13. It can be seen that the theoretical results are basically consistent with the test results, indicating that the proposed damage model is reasonable.

6. Conclusions

(1) The failure characteristics, strength, and deformation characteristics of a coarse-grained soil were analyzed, and it was found that the "bulging" phenomenon typically occurred after the failure of the sample. The deviatoric stress–strain curves of the samples in the natural and saturation states and the drying–wetting cycles appeared plasticized. The influences of the first and second cycles on the

deviatoric stress–strain curves of the coarse-grained soil are large, while the influences of the third to seventh cycles tend to be stable. The peak strain is not affected by the drying–wetting cycles and increases with increasing confining pressure. The secant modulus of the peak point decreases with increasing number of drying–wetting cycles, the initial tangent modulus decreases slightly, and the secant modulus of the peak point is not significantly affected by the confining pressure. The influence of the drying–wetting cycles on the cohesion of the coarse-grained soil is significant, the influences of the first and second drying–wetting cycles are the greatest, and the influences of the third to seventh cycles tend to be stable. The drying–wetting cycles have only a small effect on the internal friction angle

(2) Normalization was used to preprocess the deviatoric stress–strain curves of the coarse-grained soil under the drying–wetting cycles. It was found that the distribution characteristics of the deviatoric stress–strain curves of the coarse-grained soil after treatment were very similar and that the curves could be described using a hyperbolic model. A damage constitutive equation was constructed by introducing a damage variable into the hyperbolic model to reflect the influence of the number of drying–wetting cycles. The model parameters were obtained and the model was verified by fitting the experimental result

Data Availability

All the data used to support the findings of this study are available from the corresponding authors upon request.

Conflicts of Interest

The authors declare no competing interests.

Authors' Contributions

Shuyi Li and Siwei Wang wrote the main manuscript test. Zhilei He wrote the damage model. Peng Zhu, Longxi Mei, and Shaojun Zeng prepared Figures 1–11. All authors reviewed the manuscript.

References

[1] A. Ran, K. Lingwei, and L. Chengsheng, "Effects of drying-wetting cycles on the microstructure and mechanical properties of granite residual soils," *Soil Mechanics and Foundation Engineering*, vol. 58, no. 6, pp. 474–481, 2022.

[2] Z. Esfandiari, M. Ajdari, and F. Vahedifard, "Time-dependent deformation characteristics of unsaturated sand–bentonite mixture under drying–wetting cycles," *Journal of Geotechnical and Geoenvironmental Engineering*, vol. 147, no. 3, p. 04020172, 2021.

[3] R. Hao, Z. Zhang, Z. Guo, et al., "Investigation of changes to triaxial shear strength parameters and microstructure of Yili loess with drying-wetting cycles," *Materials*, vol. 15, no. 1, p. 255, 2022.

[4] N. D. Jablonowski, A. Linden, S. Koppchen, B. Thiele, D. Hofmann, and P. Burauel, "Dry–wet cycles increase pesticide residue release from soil," *Environmental Toxicology and Chemistry*, vol. 31, no. 9, pp. 1941–1947, 2012.

[5] L. Kong, H. M. Sayem, and H. Tian, "Influence of drying–wetting cycles on soil-water characteristic curve of undisturbed granite residual soils and microstructure mechanism by nuclear magnetic resonance (NMR) spin-spin relaxation time (T2) relaxometry," *Canadian Geotechnical Journal*, vol. 55, no. 2, pp. 208–216, 2018.

[6] T. P. Ngoc, B. Fatahi, and H. Khabbaz, "Impacts of drying-wetting and loading-unloading cycles on small strain shear modulus of unsaturated soils," *International Journal of Geomechanics*, vol. 19, no. 8, p. 04019090, 2019.

[7] M. Turunen, J. Hyväluoma, J. Heikkinen, et al., "Quantifying physical properties of three sphagnum-based growing media as affected by drying–wetting cycles," *Vadose Zone Journal*, vol. 18, no. 1, article 190033, 2019.

[8] S. N. Zheng, L. Qi, R. He, J. T. Wu, and Z. J. Wang, "Erosion damage and expansion evolution of interfacial transition zone in concrete under dry-wet cycles and sulfate erosion," *Construction and Building Materials*, vol. 307, p. 124954, 2021.

[9] G. T. Zhao, Z. Han, W. L. Zou, and X. Q. Wang, "Evolution of mechanical behaviours of an expansive soil during drying-wetting, freeze-thaw, and drying-wetting-freeze-thaw cycles," *Bulletin of Engineering Geology and the Environment*, vol. 80, no. 10, pp. 8109–8121, 2021.

[10] D. Hua-feng, X. Yao, F. Jing-cheng, Z. Heng-bin, W. Chen-xi-jie, and C. Yi, "Shear strength degradation and slope stability of soils at hydro-fluctuation belt of river bank slope during drying-wetting cycle," *Rock and Soil Mechanics*, vol. 38, no. 9, pp. 2629–2638, 2017.

[11] J. Xu, Y. F. Li, S. H. Wang, Q. Z. Wang, and J. L. Ding, "Shear strength and mesoscopic character of undisturbed loess with sodium sulfate after dry-wet cycling," *Bulletin of Engineering Geology and the Environment*, vol. 79, no. 3, pp. 1523–1541, 2020.

[12] H. Yan-zhou, W. Tie-hang, C. Lei, and J. Xin, "Structural constitutive relation of compacted loess considering the effect of drying and wetting cycles," *Rock and Soil Mechanics*, vol. 42, no. 11, pp. 2977–2986, 2021.

[13] Y. Liu, Z. Zhu, and J. Chen, "Experimental research on static mechanical properties of cement-improved argillite-slate coarse-grained soil under drying-wetting cycles," *Journal of Central South University*, vol. 50, no. 3, pp. 679–686, 2019.

[14] C. Leqiu, C. Junhua, and Z. Jiasheng, "Drynamic properties of cement-improved argillite-slate coarse-grained soil under drying-wetting cycles," *Journal of Hunan University (Natural Sciences)*, vol. 44, no. 9, pp. 107–113, 2017.

[15] X. Jian, W. Zhi-peng, and C. Hui, "Triaxial shear behavior of basalt fiber reinforced loess under drying-wetting cycles," *Rock and Soil Mechanics*, vol. 43, no. 1, pp. 28–36, 2022.

[16] H. Xuhui, Z. Kunyong, N. Meijun, and P. Renyou, "Effect of experimental conditions on strength indexes of expansive soil during wet–dry cycles," *Journal of Central South University (Science and Technology)*, vol. 53, no. 1, pp. 269–279, 2022.

[17] T. Chaosheng and S. Bin, "Swelling and shrinkage behaviour of expansive soil during wetting-drying cycles," *Chinese Journal of Geotechnical Engineering*, vol. 33, no. 9, pp. 1376–1384, 2011.

[18] D. Jinyu, Z. Zhiqiang, Y. Jihong, and H. Zhiquan, "Research on the deformation evolution and the strength weaking of slip soil

under wetting-drying cycle," *Journal of Sichuan University (Engineering Science Edition)*, vol. 48, no. S2, pp. 1–7, 2016.

[19] Z. Zhen-hua and W. Ye, "Degradation mechanism of shear strength and compressive strength of red sandstone in drawdown areas during reservoir operation," *Chinese Journal of Geotechnical Engineering*, vol. 41, no. 7, pp. 1217–1226, 2019.

[20] Z. Zhenhua, H. Xiang, and C. Qiang, "Experimental study on deterioration of the tensile strength of red sandstone during the operation of reservoir," *Chinese Journal of Rock Mechanics and Engineering*, vol. 36, no. 11, pp. 2731–2740, 2017.